Main Manuscript for

Exploring Peptide-Based Nanodiscs Structure and Dynamics through Synergistic Approach of NMR Spectroscopy, SAS and MD Simulations

Sirine Nouri,*[1] Akseli Niemelä,[1] Ricky Nencini,[1,2] Georgios Kolypetris,[1] Tuomas Niemi-Aro,[2] Salla I. Virtanen,[2] O. H. Samuli Ollila,[2,3] and Artturi Koivuniemi,*[1]

[1]Division of Pharmaceutical Biosciences, Faculty of Pharmacy, University of Helsinki, Helsinki, Finland
[2]Institute of Biotechnology, University of Helsinki, Helsinki, Finland
[3]VTT Technical Research Centre of Finland, Espoo, Finland

*Corresponding authors

Email: sirine.nouri@helsinki.fi, artturi.koivuniemi@helsinki.fi

Competing Interest Statement: The authors declare that they have no known competing financial interests or personal relationships that could have appeared to influence the work reported in this paper.

Keywords: structural biology, apolipoprotein, mimetic-peptide, therapeutics

Abstract

Peptide-based nanodiscs are promising anti-atherosclerosis biologics, drug delivery particles and structural biology tools. However, the structural and dynamic properties of these peptide-based nanodiscs remains unknown, hindering their development for the aforementioned purposes. Here we integrated molecular dynamics (MD) simulations with nuclear magnetic resonance (NMR), small-angle x-ray scattering (SAXS), and small-angle neutron scattering (SANS) experiments to investigate the structure and dynamics of therapeutic peptide-based nanodiscs constituted of DMPC phospholipids and the amphiphilic apolipoprotein A-I mimetic peptide 22A. This multi-technique approach reveals the intrinsic polydispersity in size of peptide-based nanodiscs and the need for careful interpretation of averaged experimental parameters. It also demonstrates the value of benchmarking MD simulations against multiple experimental observables to validate the computational protocol and the applied force field. We obtained a description of the nanodiscs with MD simulations that is consistent with the structural information obtained from both experimental methods: averaged size and shape of the nanodiscs from SAS and peptide site-specific information from NMR spectroscopy. Our results indicate that the nanodiscs have an average size of 90 DMPC phospholipids and 18 22A peptides with a predominantly disordered peptide orientation around the lipid matrix. The terminal regions of the peptides display greater flexibility relative to the peptide core and an enhanced C-terminal exposure to solvent, particularly at K22, a residue implicated in LCAT activation. The approach described in this paper can be used in the optimization of peptide-lipid stoichiometry and peptide sequence for therapeutic and biophysical applications.

Significance Statement

We give a structural and dynamic description of peptide-based nanodiscs composed of phospholipids and the amphiphilic apolipoprotein A-I mimetic peptide 22A via the integration of molecular dynamics (MD) simulations with nuclear magnetic resonance, small-angle x-ray scattering (SAXS), and small-angle neutron scattering (SANS) experiments. Our findings suggest that the nanodiscs display size polydispersity in the sample and that 22A peptides are disordered on the edge of the disc with enhanced C-terminal end flexibility and exposure to solvent to allow interaction with the enzyme LCAT.

Main Text

Introduction

Peptide-based nanodiscs are discoidal membrane mimetics composed of a phospholipid bilayer stabilized by amphiphilic peptides. These small particles, with diameters ranging from 6 to 20 nm, play a powerful role in therapeutic applications as they can mimic high-density lipoprotein (HDL) particles. HDL particles possess protective features against atherosclerosis as they are responsible for the removal of excess cholesterol from peripheral tissues in a process known as reverse cholesterol transport (1). However, the use of natural HDL particles is limited by the difficulties of producing large quantities of apolipoprotein A-I (apoA-I), the major protein component of HDL particles (2). To overcome this limitation, pharmaceutical research focused on the development of apoA-I mimetic peptide-based nanodiscs of tunable composition, size and morphology (3–5). These peptide-based nanodiscs can also be used as a versatile platform for targeted drug delivery as they are able to carry different molecules such as hydrophobic drugs and snRNA embedded into their lipid matrix (6). In addition to their therapeutic applications, nanodiscs are useful in structural biology research as they can stabilize membrane protein in a native-like amphiphilic environment (7, 8).

Despite the high biophysical and pharmaceutical importance of peptide-based nanodiscs, detailed knowledge of the structure and dynamics of these particles is lacking. Understanding the molecular basis of peptides' arrangement and dynamics in the nanodiscs is crucial to design more stable and

effective therapeutic nanodiscs to mimic HDL functions. Unlike nanodiscs formed with membrane scaffold proteins (MSPs), in which it was shown that a lipid bilayer is surrounded by a double belt of two MSPs (9), the number of peptides and their arrangement with respect to lipid in peptide-based nanodiscs is not well understood. So far, most of the peptide-based nanodisc studies focused on the peptide 18A, which was designed to mimic the amphiphilic helical motif of apoA-I (10–12). These studies reported that the peptides are arranged on the perimeter of the disc. There is no general agreement about a structural model describing the arrangement of apoA-I mimetic peptides in nanodiscs as it strongly depends on the physicochemical properties of the peptides. For example, it is not understood how the sequence of the peptide and its length impact its ability to form dimers or oligomers in the rim of nanodiscs and, further, how this affects the stability of nanodiscs. Therefore, in order to design better apoA-I mimetic peptide-based nanodiscs for therapeutical and structural biology use, the structural and dynamic properties of apoA-I mimetic peptides in complex with phospholipids must be characterized.

In the present study, we investigate nanodiscs made with the apoA-I mimetic peptide 22A (Esperion Therapeutics, ESP24218) (13). This peptide was optimized to activate plasma enzyme lecithin:cholesterol acyltransferase (LCAT) when bound to nanodiscs. LCAT esterifies cholesterol on the surface of HDL during reverse cholesterol transport and is responsible for the formation of spherical HDL particles (14). To our knowledge, no detailed molecular and structural description has been reported on this system. Previously, we have found based on molecular dynamics (MD) simulations that the C-terminal end of 22A interacts with the lid-binding groove of LCAT in the open state (15, 16). Particularly, the C-terminal lysine K22 seems to be an important residue for LCAT activation as its removal significantly reduces the cholesterol esterification activity of LCAT (17). Nevertheless, the organization of 22A peptides in the rim of nanodiscs is not known experimentally.

Nuclear magnetic resonance (NMR) spectroscopy and small angle scattering (SAS) are two complementary techniques to study biomolecular complexes as peptide-based nanodiscs (18, 19). NMR relaxation data provides atomistic, site-specific information about the peptides and can probe motions on the picosecond to nanosecond timescale; yet it does not give direct information about the lipids. Instead, small angle X-ray scattering (SAXS) and small angle neutron scattering (SANS) data contain information from both peptides and lipids and report on the average size and shape of the nanodiscs (20). These experimental data provide independent structural information on the nanodiscs, but their direct interpretation is challenging as conventional approaches are not suited for the study of biomolecular complexes (18, 21). MD simulations can be used to generate conformational ensembles of the nanodiscs at the atomic level, although the results will be dependent on the computational protocol and the applied force field. Thus, MD simulations must be validated against experimental data to assess their accuracy (22). The integrative approach of combining local and global information from NMR and SAXS experiments with MD simulations is a very robust method to overcome the limitations of individual structural techniques and to form a more complete picture of the structure and dynamics of peptide-based nanodiscs.

Here, we combined experimentally determined NMR relaxation parameters and SAXS and SANS profiles with multiple MD simulations to describe the molecular composition of 22A peptide-based nanodiscs and the peptides flexibility in the rim of the nanodiscs. We obtained a model of the peptide-based nanodiscs that is consistent with the structural information obtained from each method and gives structural information on the interaction of these nanodiscs with the enzyme LCAT.

Results

Experimental characterization of peptide-based nanodiscs

Nanodiscs composed of 22A peptides and DMPC phospholipids with a 1:5 peptide/lipid molar ratio were prepared following our previously developed protocol (15). Dynamic light scattering (DLS) was used to characterize the size distribution profile of the particles in the sample (Fig.1A). A single

peak with a volume-averaged size of 8.4 ± 1.0 nm was observed, corresponding to correctly assembled nanodiscs. No large lipid aggregates were detected. The helical content of 22A in a free form and in nanodiscs was measured by circular dichroism (CD) (Fig. 1B). In both free form and in the nanodiscs, 22A was mostly helical (79.7 ± 1.2 % and 81.7 ± 1.3 % respectively). The transmission electron microscopy (TEM) image shows the typical discoidal morphology of the nanodiscs (Fig. 1C). Size exclusion chromatography (SEC) was performed to quantify the repartition of peptide in the sample. One predominant symmetric peak was observed in the chromatogram with a retention volume around 13 mL (Fig. 1D), indicating the correct formation of nanodiscs and the absence of free peptides in solution. Based on these characterizations, we confirmed the correct formation of nanodiscs in the sample, but we also observed heterogeneity in size of the nanodiscs, as reported in other studies (5, 20). We hypothesized that it corresponds to a distribution in the number of lipids and peptides incorporated in the nanodiscs while respecting the 1:5 peptide/lipid molar ratio.

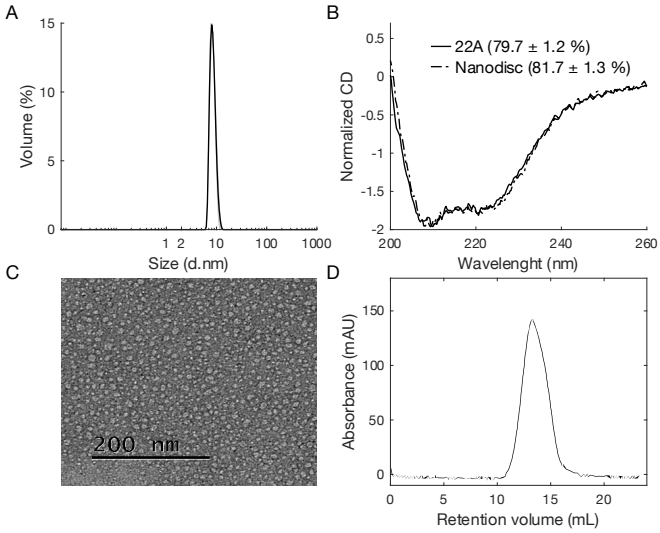

Figure 1. Characterization of a peptide-based nanodisc sample. (A) DLS measurement of the nanodiscs size. (B) Circular dichroism spectra of lipid-free 22A and nanodiscs. (C) TEM image of nanodiscs. (D) Size exclusion chromatography profile of nanodiscs.

Nanodiscs for NMR experiments were prepared using two differently labeled 22A peptides with ^{15}N labels in all leucine residues [L-^{15}N] or with the specifically labeled residues [R_7-A_{16}-K_{18}-^{15}N-^{13}C] (Fig. 2A). All peaks were well resolved in ^{1}H-^{15}N-HSQC spectrum for both samples and each peak was successfully assigned to a residue (Fig. 1D), suggesting the absence of conformational exchange with significantly populated conformers with dynamics slower than the millisecond timescale. Nuclear spin relaxation parameters, T_1, T_2 and heteronuclear ^{1}H-^{15}N NOE, from ^{15}N labeled amino acids are shown in Fig. 2B. Overall, the relaxation data are rather uniform between residues, yet showing a bell-shape dependence along the sequence, indicating a different flexibility between both termini and the internal residues.

SAXS data were measured for nanodisc samples at 0.12, 0.25, 0.5 and 1 mg/mL peptide concentration (Fig. S2). All scattering curves overlap at low scattering angles indicating no aggregation or interparticle effect in this concentration range. The scattering curve at 1 mg/mL peptide concentration (Fig. 2C) is used in the rest of the study as it has the lowest measurement noise. The scattering curve exhibits a flat region at low q values, a local minimum around 0.07 $Å^{-1}$ and a broad bump at higher q values. This trend is characteristic for nanodisc solutions due to the complex scattering contrast situation, with positive excess scattering length density from the lipid headgroups and the peptides and negative excess scattering length density from the lipid

hydrophobic alkyl chains (23). This is also observed in the pair-distance distribution functions P(r) (Fig. 2D), which represent the distribution of intramolecular distances within the molecular envelope. Based on SAXS P(r), the maximum distance in the nanodisc is around 12 nm, which is in good agreement with the DLS data.

SANS data were recorded on a nanodisc sample at 1 mg/mL peptide concentration in a 100 % D_2O buffer (Fig. 2C). The 100 % D_2O SANS data contains negative excess scattering length densities from both the peptides and the lipids. The scattering curve displays a flat region at low q values and then a decay. SANS P(r) is also indicating a maximum distance of around 12 nm in the nanodisc (Fig. 2D).

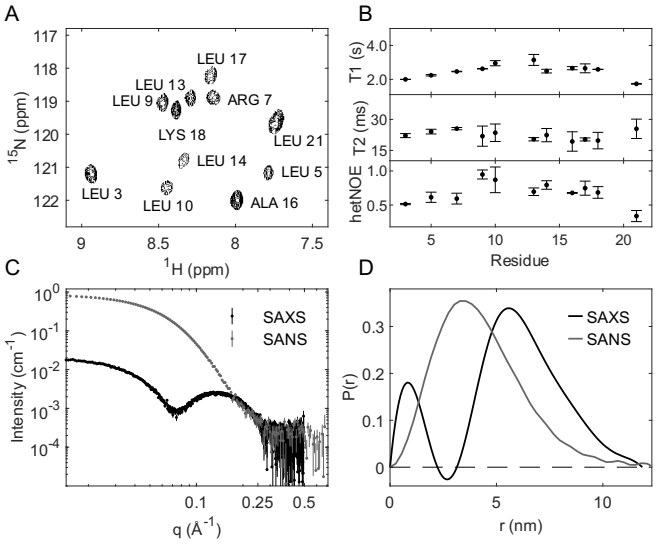

Figure 2. NMR and SAXS experimental data of peptide-based nanodiscs. (A) ^{1}H-^{15}N HSQC NMR spectrum. Superposition of two ^{1}H-^{15}N HSQC spectra from [L-^{15}N] and [R_7-A_{16}-K_{18}-^{15}N-^{13}C] labeled samples. Assignment is indicated. (B) ^{15}N relaxation parameters. Data are represented as mean ± SD of duplicate measurements. (C) Scattering data at 1 mg/mL peptide concentration. (D) Pair-distance distribution function derived from the scattering data. All experimental data were measured at 310 K.

Molecule count in nanodiscs from simulation-experiment integration

Results from DLS and SEC indicated that all peptides and lipids are incorporated into the nanodiscs, supporting the assumption of a 1:5 peptide/lipid ratio. However, experimental methods cannot directly determine the absolute number of molecules per nanodisc. Therefore, we performed MD simulations with varying numbers of lipids and peptides while maintaining the 1:5 ratio, then compared simulation results to experimental data to identify the most physically reasonable nanodisc size. We simulated nanodiscs with 50, 70, 90 and 110 DMPC lipid molecules and 10, 14, 18, and 22 22A peptide molecules, respectively, with the AMBER force field. These simulations are named MD 50, MD 70, MD 90 and MD 110 in this paper. Each system was simulated for at least 3 µs and repeated three times from different initial configurations, as described in Table S1.

We observed systematic changes in the calculated T_1 and T_2 values with nanodisc size: T_1 values increased with larger nanodiscs while T_2 values decreased. No such systematic change was observed for the hetNOE values. The simulation system MD 70 reproduces the T_1, T_2, and hetNOE experimental spin relaxation times with the best agreement in comparison with MD 50 and MD 90 (Fig. 3A, Table 1). For SAS data, there are visible modifications of the shape of the calculated I(q)

when changing the size of the nanodisc. For SAXS, when the size of the nanodisc increases the intensity of the low q values is higher, the local minimum is shifted towards smaller q values and the shape of the broad bump at higher q values changes. For SANS, the intensity of the low q values is also higher when the size of the nanodisc increases and the curvature of the decay is affected. The simulation system MD 90 gives the best representation of the experimental SAXS and SANS data in comparison with MD 70 and MD 110 (Fig. 3B, Table 1).

The discrepancy between simulation systems representing experimental data can be explained by the size polydispersity of the nanodiscs in the sample. In an NMR spectrum, the signal of a peak obtained for one residue corresponds to the averaged signal from this residue in all 22A peptides present in nanodiscs of different sizes. However, the peak width of a residue is inversely proportional to T_2 (24). As seen in Fig. 3A, T_2 values are decreasing when the size of the nanodisc increases. Thus, a 22A residue in a large nanodisc has a broader NMR peak and therefore a lower intensity than a 22A residue in a smaller nanodisc. Smaller nanodiscs have a bigger weight in the calculation of the averaged NMR signal in comparison with larger nanodiscs. To have a better understanding of this trend, we plotted the averaged T_2 value from residues 10 to 14 (Fig. 3C) against the size of the nanodisc for MD simulations of different composition. We fitted these points with a power function ($y = 16.9\ x^{-3.3}$, $R^2 = 0.94$) and used this function to rescale the experimental DLS size distribution to get a size distribution “as seen” by NMR spectroscopy (Fig. 3D). As expected, the size distribution maximum is shifted towards smaller particles, from around the size of 90 lipids nanodiscs to the size of 70 lipids nanodiscs. Overall, we obtained a description of the nanodiscs with MD simulations that is consistent with the structural information obtained from NMR and SAS experimental methods. Our results suggest that the sample is composed of nanodiscs with different sizes, with nanodiscs ranging from around 50 lipids to more than 110 lipids, and in average, that the nanodiscs are constituted of 90 lipids and 18 22A peptides.

	MD 50	MD 70	MD 90	MD 110	MD CHARMM
χ^2 - T1	0.64	0.44	1.24	N/A	0.62
χ^2 - T2	1.41	0.45	0.98	N/A	0.68
χ^2 - hetNOE	0.73	0.58	0.53	N/A	0.84
χ^2 - SAXS	N/A	12.14	3.54	3.91	4.10
χ^2 - SANS	N/A	26.98	4.80	5.35	5.50

Table 1. Agreement between MD simulations and experiments.

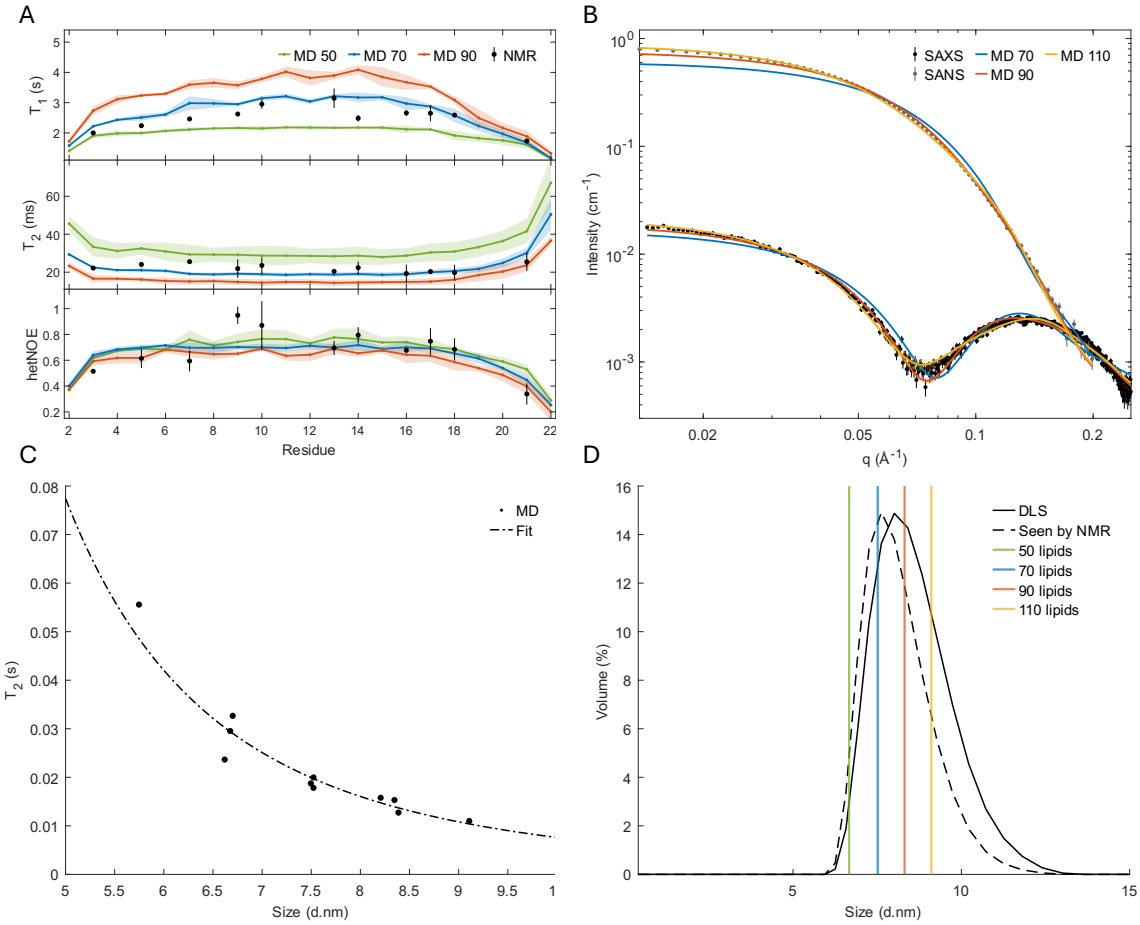

Figure 3. Comparing MD simulations of nanodiscs with different sizes with experiments. (A) NMR relaxation parameters. (B) SAXS and SANS curves. MD data are represented as mean ± SD of triplicate simulations. (C) Correlation between T_2 values and size of nanodiscs, both calculated from MD simulations. The fitted trendline corresponds to a power function ($y = 16.9\ x^{-3.3}$, $R^2 = 0.94$). (D) DLS experimental size distribution of the nanodiscs (solid black line) and rescaled distribution "as seen" by NMR (dashed black line). Vertical lines correspond to the hydrodynamic diameters of the nanodiscs calculated from MD simulations.

Flexible peptides in simulations achieve better agreement with experimental data

We investigated the impact of the force field on the ability of MD simulations to reproduce experimental data. We run MD 70 (for NMR parameters) and MD 90 (for SAS) simulations with the CHARMM force field (MD 70 CHARMM, MD 90 CHARMM) and compare them with the simulations with the AMBER force field (MD 70, MD 90). No difference was observed for SAXS and SANS curves between the two force fields (Fig. 4B). For the NMR relaxation parameters (Fig. 4A), we observed that T_1 and T_2 have similar values for both force fields from residues 6 to 18. For the N-terminal and especially the C-terminal residues, the CHARMM force field gives smaller T_1 and higher T_2. For the whole peptide, smaller hetNOE are observed with the CHARMM force field. The AMBER MD simulation better describes the flexibility of the peptides end by following the bell-shape dependence along the sequence whereas CHARMM gives a more rigid description of the peptides end inside the nanodisc.

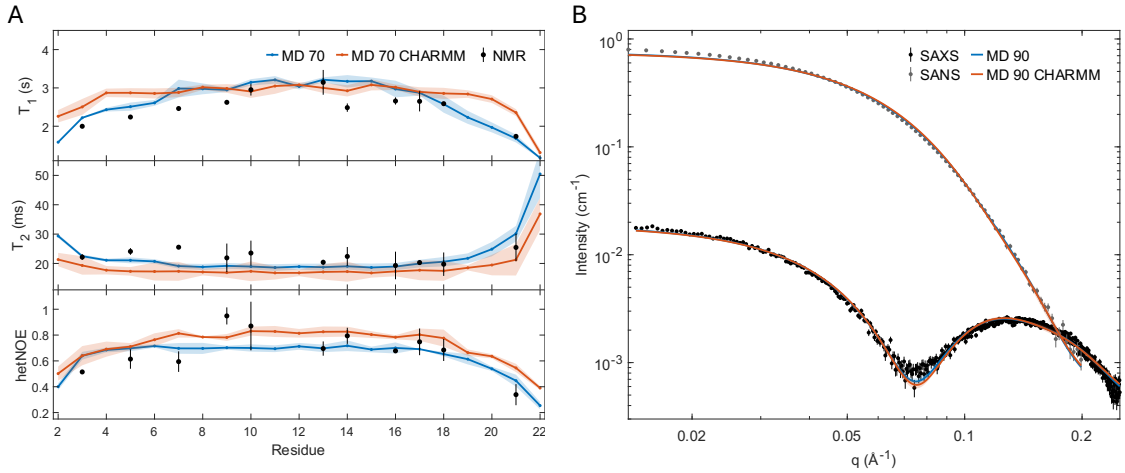

Figure 4. Effect of force field on the reproduction of experimental data from MD simulations. (A) NMR relaxation parameters. (B) SAXS and SANS curves. MD data are represented as mean ± SD of triplicate simulations.

Peptide behavior under different force fields was further characterized. We first calculated the per residue solvent accessible surface areas (SASA) (Fig. 5A and Fig. S3A). As expected for amphiphilic peptides, hydrophobic amino acids have lower SASA values as they face the hydrophobic acyl chains of the phospholipids (V2, L3, F6, L9, L10, L13, L14, A16 and L17), while hydrophilic amino acids are more exposed to solvent. Notably, the C-terminal residue L21 has a higher SASA value than the other leucines in the sequence and the residue K22 is highly exposed to the solvent. We then characterized the flexibility of the peptides with the calculation of the backbone root mean square fluctuations (RMSF) per residue (Fig. 5B and Fig. S3B). All residues have similar RMSF values, except for N-terminal residues P1 and V2 and especially C-terminal residues K20, L21 and K22 that have higher RMSF values, which means that they are more flexible. Overall, the peptides were more rigid under the CHARMM force field than the AMBER force field.

Peptide orientation in nanodiscs from simulation-experiment integration

In our initial configurations, created from coarse-grained self-assembly simulations, substantial peptide ordering was not observed. Atomistic simulations retained this disorder and showed good agreement with NMR and scattering data. However, a previous simulation study suggested a picket fence-like peptide orientation, with peptides aligned parallel to the lipid bilayer normal at the nanodisc rim (25). To investigate whether the picket fence configuration would also agree with experiments, we performed MD 70 and MD 90 simulations using CHARMM and AMBER force fields with starting structures where peptides were ordered at the disc edge in a picket fence arrangement. In AMBER force field simulations, peptides did not maintain the picket fence configuration but reoriented into a more random arrangement, indicating that this conformation is unstable. Conversely, in CHARMM force field simulations, peptides remained in the picket fence configuration throughout the entire simulation.

We observed no differences in NMR relaxation parameter reproduction between MD 70 CHARMM simulations with and without the picket fence configuration (Fig. S4A and Table S2). However, for SAXS and SANS data, the MD 90 CHARMM simulation with disordered peptide configuration showed better experimental agreement than simulations with the picket fence configuration (Fig. S4B and Table S2). A similar comparison was not feasible for AMBER simulations because the picket fence configuration was unstable.

In conclusion, AMBER simulations with more disordered peptides and unstable picket fence configurations show better overall agreement with experimental data than CHARMM simulations

where the picket fence configuration remains stable. These results suggest that 22A peptides in nanodiscs are more likely disordered at the disc edge rather than ordered in a picket fence conformation. We observed in Fig. 5C and Fig. 5D that the peptides are arranged in the rim of the nanodiscs with the C-terminal ending, and particularly the final residue K22, pointing toward the solvent and thus being available for interaction with LCAT. Overall, the peptides behavior is similar in MD 70 and MD 90.

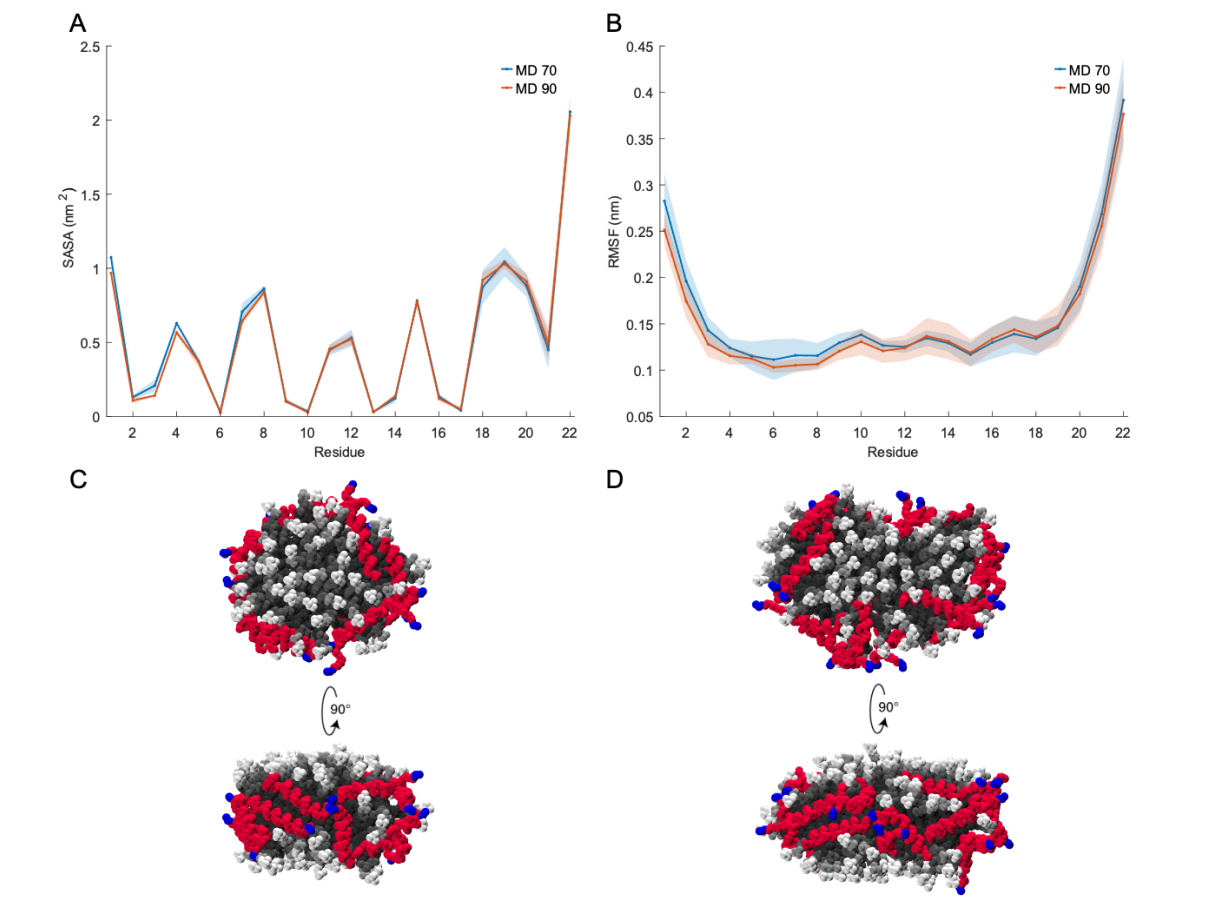

Figure 5. Analysis of the MD simulations. (A) Solvent accessible surface area (SASA) per residue. (B) Root mean square fluctuation (RMSF) per residue. MD data are represented as mean ± SD of triplicate simulations. (C) Snapshot of MD 70 simulation, top view and side view. (D) Snapshot of MD 90 simulation, top view and side view. DMPC phospholipids are colored in greyscale, 22A peptide in red with residue 22 in blue.

Discussion

In this study, we combined experimental biophysical characterization and MD simulations to provide an integrated description of peptide-based therapeutic nanodiscs assembled from 22A peptides and DMPC phospholipids. We aimed to understand how apoA-I mimicking 22A peptides are organized and how they interact with lipids in nanodiscs as those features are likely important regarding their biological activities and stability. Multiple complementary techniques confirmed the successful assembly of discoidal nanodiscs with minimal aggregation and 22A peptides being predominantly in α-helical configuration when bound to lipids. However, DLS and SEC data revealed a certain degree of size heterogeneity. Such polydispersity likely arises from the flexible stoichiometry of peptide incorporation. Contrary to MSP nanodiscs, where the size of the nanodiscs

is constrained by the fixed size of the MSP belt (7), in peptide-based nanodiscs, the peptides do not confine the size of the formed nanodiscs as different amounts of peptide molecules can be incorporated to the nanodiscs. For example, it has been shown that the average size of peptide-lipid nanodiscs can be modulated by peptide-lipid ratio and temperature (26).

Our combined approach of using MD simulations, NMR, SAXS and SANS data provided structural and dynamic information on the nanodiscs under physiologically relevant conditions. The overall levels of T_1 and T_2 profiles in different simulations were following the size of the nanoparticles in MD simulations indicating that the overall rotation of nanodiscs determines the averaged levels of T_1 and T_2 relaxation values in our nanodisc systems. The bell-shaped residue dependence of the NMR relaxation parameters was determined by the local peptide flexibility, with the terminal regions displaying greater flexibility relative to the peptide core. The overall level and the bell-shaped curve of NMR relaxation results matched well with the simulated nanodisc consisting of 70 DMPC phospholipids and 14 22A peptides whereas the nanodisc consisting of 90 DMPC phospholipids and 18 22A peptides more closely reproduced the SAS profiles. We concluded that the observed NMR relaxation signal is primarily dominated by smaller-sized nanodiscs, whereas the SAS profiles reflect the entire heterogeneous nanodisc population. This emphasizes the absolute need to use complementary techniques such as NMR spectroscopy and SAS when studying complicated polydisperse systems as peptide-based nanodiscs. More monodisperse samples could be prepared using techniques such as size-exclusion chromatography, gradient ultracentrifugation, and asymmetric flow field-flow fractionation (27, 28). However, implementing such approaches for isotope-labelled peptide-nanodisc samples would likely incur a substantial cost due to the large quantities of isotope labelled peptides required.

Atomistic simulations are computationally challenging for nanodiscs because they require large boxes to accommodate the peptide-lipid complex. Thus, only few studies have characterized peptide-based nanodiscs or nanodiscs formed with MSP at atomistic resolution. Most of them have used a version of the CHARMM force field (CHARMM22, CHARMM36 and CHARMM36m) (25, 29–31) while one study used the AMBER ff99SB-ILDN force field (32). In our case, when comparing simulations with the AMBER ff99SB-ILDN and the CHARMM36m force fields, it was evident that NMR relaxation parameters were better reproduced by the AMBER simulations than the CHARMM simulations, especially for the terminal residues. The CHARMM force field gives a more rigid description of the peptides inside the nanodisc as shown with the RMSF calculations. Nevertheless, the AMBER and CHARMM simulations yielded nearly identical SAS curves, indicating that large-scale shape and size descriptors are less sensitive to the force field choice when compared to local peptide dynamics.

Concerning the spatial organization of peptides around the lipid matrix, a study showed that class A amphipathic peptides are arranged in the rim of the nanodiscs in a double belt arrangement (33) as adopted by apoA-I in discoidal HDL particles (34). One group challenged this arrangement when they studied four different apoA-I mimetic peptides by MD simulations and showed that these peptides are arranged in a vertical picket fence configuration in the nanodiscs (25), although experimental evidence is missing in this study. Here, we showed that the more ordered picket fence configuration was not stable in the AMBER simulation, as this conformation relaxed toward a disordered organization. In the CHARMM simulation, the system maintained the ordered conformation better. Despite this structural persistence in CHARMM, disordered arrangement is in better agreement with SAS experiments than the picket fence configuration. The NMR relaxation values were not changed by the spatial organization of peptides. Therefore, considering all these results together, 22A peptides likely adopt a more disordered orientation around the rim of the nanodisc rather than a stable, symmetric arrangement.

SASA and RMSF analysis showed that the terminal ends of 22A peptides are clearly more exposed to solvent and more dynamic when compared to the mid-region. Interestingly, SASA profiles indicated that although the N- and C-terminal ends are more dynamic, only the C-terminal end residue L21 showed increased SASA when compared to other hydrophilic leucines in the 22A

peptide sequence. This indicates that due to the C-terminal end flexibility, L21 and K22 are occasionally exposed to water when other leucines are solely interacting with lipids. Previously, it has been reported that the C-terminal end residue K22 of 22A is important in LCAT activation, as either deletion or substitution of K22 has been shown to reduce the peptide's ability to activate LCAT (15, 17). Our simulation trajectories show that the C-terminal end K22 is well exposed to water and not bound to phospholipid surface. We hypothesize that this water exposure or more loose structure could be an important factor in the interaction with LCAT.

In conclusion, our results demonstrate that the integration of NMR and SAS experimental techniques with MD simulations provides a more coherent picture of the structural and dynamic heterogeneity of peptide-based nanodiscs. The ability of MD simulations to reproduce different experimental observables at different nanodisc sizes highlights the intrinsic polydispersity of these systems and underscores the need for careful interpretation of averaged experimental parameters. Furthermore, the differences observed between the AMBER and CHARMM force fields underlines the importance of benchmarking simulations against high-resolution experimental data when investigating flexible biomolecular assemblies. Our combined approach could be used to systematically assess how peptide sequence variations, nanodisc lipid composition, temperature, or peptide-to-lipid ratios influence nanodisc size distributions and peptide flexibility, paving the way for more accurate structural and dynamic description of polydisperse peptide-based nanodisc systems. This knowledge can be used in optimizing stoichiometry and molecular architecture for specific therapeutic or biophysical applications.

Materials and Methods

Sample preparation

Two apoA-I mimetic peptides 22A (PVLDLFRELLNELLEALKQKLK) with different isotopic labels in leucines [L-^{15}N] or in selected amino acids [R_7-A_{16}-K_{18}-^{15}N-^{13}C] were obtained in powder form from Peptide Protein Research Ltd (Fareham, UK). Deuterated 1,2-Dimyristoyl-sn-glycero-3-phosphocholine (DMPC) lipids were purchased in powder form from Avanti Polar Lipids Inc. (Alabaster, USA). 260 µL of a 5 mg/mL stock solution of DMPC phospholipids dissolved in chloroform was dried with a Rotavapor R-200 (BUCHI Labortechnik, Flawil, Switzerland) for one hour at room temperature. The resulting white thin lipid film was rehydrated in 1 mL of 1/50 X PBS buffer (pH 7.4). The solution was vortexed for 5 minutes and then sonicated in a water bath for one hour to obtain a clear liposome solution. 200 µL of a 5 mg/mL stock solution of labeled 22A peptides dissolved in 1/50 X PBS buffer (pH 7.4) was added. The sample was heated at 50°C for 5 minutes and then cooled to 4°C for 5 minutes. The heating-cooling cycle was repeated three times. The sample was concentrated on a Vivaspin 50k centrifugal tube (Sartorius) to reach a volume of 500 µL. 10% (v/v) D_2O was added. The sample was transferred to a 5 mm NMR tube. The final peptide concentration is 0.75 mM and the stoichiometry is 5 phospholipids per peptide.

In total, four samples were produced: two samples were [L-^{15}N] labeled and two samples were [R_7-A_{16}-K_{18}-^{15}N-^{13}C] labeled. One of the [L-^{15}N] labeled sample was fully characterized as described in the following section.

Sample characterization

All experimental data were measured at 310 K, above the melting temperature of DMPC (297.1 K) where the lipids are expected to be in liquid phase.

Dynamic light scattering (DLS) (Zetasizer APS, Malvern Instruments, Westborough, MA) was used to characterize the size of the nanodiscs at 310 K. The results are shown as volume distribution of hydrodynamic diameters. Data are represented as the average of three measurements.

369 The helical content of lipid-free peptide and peptide in the nanodiscs was measured with a J-815
370 circular dichroism spectropolarimeter (Jasco). Samples were measured in a 20 mM phosphate
371 buffer, pH 7.4 with a final peptide concentration of 0.01 mg/mL. The sample temperature was kept
372 at 310 K during measurement using a Peltier temperature controller. 4 mL of sample were placed
373 in a quartz cuvette with a path length of 1 cm. Data were acquired over a wavelength range of 200–
374 260 nm with a data interval of 0.2 nm and a scanning speed of 100 nm/min. Four scans were
375 averaged for each sample. The percentage of helix was estimated using the CDPro analysis
376 software with the program CONTIN (35).

377 The morphology of the nanodiscs were observed via transmission electron microscopy (TEM) on
378 a Hitachi HT7800 electron microscope. The sample was diluted in a 20 mM HEPES, 120 mM NaCl,
379 1 mM EDTA buffer to obtain a final peptide concentration of 0.10 mg/mL. 3 µL of the sample was
380 applied on an EM grid (200 mesh Cu + continuous carbon) for 45 seconds. The grid was washed
381 three times with ultrapure water and blotting with filter paper before each wash. Negative staining
382 with 2% uranyl acetate was performed first for 5 seconds and then for 60 seconds. The filter paper
383 was used to blot the grid before the stain was applied and after the final staining. The grid was air-
384 dried for 5 minutes. The microscope was operated at 100 kV voltage at a magnification of 40kX.
385 The resulting pixel size was 2.8 Å/pixel.

386 Size exclusion chromatography was used to assess the purity of the nanodiscs. The sample was
387 eluted through a Superdex 200 Increase column by 1X PBS (pH 7.4) with an isocratic flow rate of
388 0.4 mL/min and detected at 200 nm.

389 **NMR spectroscopy**

390 NMR measurements were performed on a Bruker 850 MHz Avance III HD spectrometer, equipped
391 with a cryogenically cooled TCI triple-resonance probe, at the Finnish Biological NMR Center. All
392 experiments were measured at 310 K. [^{15}N,^{1}H]-HSQC, [^{1}H,^{1}H]-TOCSY, and ^{1}H NOESY
393 experiments were used for the assignment of the labeled peptide residues, as described previously
394 (36). The ^{1}H NOESY mixing time was set to 280 ms. TROSY-based NMR pulse sequences (37)
395 were used to measure the longitudinal (T_1) and transverse (T_2) relaxation times and the
396 heteronuclear nuclear Overhauser effects (NOE) of ^{15}N nuclei in N-H groups. Series of two-
397 dimensional spectra were recorded with different delays to determine relaxation rate constants.
398 The following delays were used: T_1 delays of 50, 150, 300, 500, 800, 1000, 1500 and 3000 ms and
399 T_2 delays of 16, 32 and 48 ms. Two heteronuclear NOE spectra were recorded with and without
400 proton saturation during relaxation delay. All data sets were acquired using 128 scans and 32
401 increments with a recycle delay of 3.5 s. T_1, T_2 and hetNOE data were measured from all four
402 samples providing two independent values for each spin relaxation observable.

403 Spectra were processed using nmr-Pipe (38). CcpNmr (39) was used to determine the intensities,
404 in arbitrary units, for the amide ^{1}H-^{15}N cross peaks by measuring the height of the peaks. Intensities
405 of cross peaks were fitted to single exponential functions to determine relaxation rate constants T_1
406 and T_2 (Fig. S1). Heteronuclear NOE values were obtained by taking the ratio of the intensities
407 measured in the spectra collected with and without proton saturation. Error bars were calculated
408 as standard deviation from relaxation measurements done on two independently prepared
409 samples.

410 **SAXS and SANS measurements**

411 SAXS and SANS data were performed at the BM29 BioSAXS beamline (40) at the European
412 Synchrotron Radiation Facility (ESRF) and at the D22 beamline at the Institute Laue-Langevin
413 (ILL), respectively, in Grenoble, France. The scattering intensity, I(q), was measured as a function
414 of $q = 4\pi\sin(\theta)/\lambda$, where q is the scattering vector, 2θ is the scattering angle, and λ is the X-
415 ray/neutron wavelength. Both the SAXS and SANS measurements were done at 37°C.

For the SAXS measurements, the nanodisc sample was measured in 1/50 X PBS buffer (pH 7.4), at four peptide concentrations (0.12, 0.25, 0.5 and 1 mg/mL) to avoid inter-particle interactions, at an X-ray energy of 12.5 keV. With λ = 0.99 Å and a sample-detector distance of 2.8 m, data were obtained in the q-range from 0.0085 $Å^{-1}$ to 0.494 $Å^{-1}$. Ten SAXS frames of 1 second were averaged, background subtracted and normalized to absolute scale units (cm^{-1}) using water as calibration standard(41) with the data reduction software ScÅtter (42).

For the SANS measurements, the usual H_2O based buffer was substituted with a corresponding buffer with 100% D_2O. The nanodiscs sample at 1 mg/mL peptide concentration was placed in a Hellma quartz cuvette (1 mm path). The instrument was set up with a neutron wavelength of 6 Å +/- 10%, a collimation length of 5.6 m and two different sample-detector distances, 1.4 m and 5.6 m, yielding data in the q-range from 0.0094 $Å^{-1}$ to 0.69 $Å^{-1}$. The data reduction was performed according to standard ILL procedures by applying corrections for detector sensitivity, electronic noise, and empty cell scattering. The intensity was normalized to absolute scale units (cm^{-1}) using the flux of the direct beam. Buffer subtraction was done with IGOR Pro.

Pair-distance distributions were calculating using GNOM from the ATSAS package (43).

MD simulation

To create initial structures for atomistic simulations, we initiated coarse-grained Martini 3 simulations (44) with 30, 50, 70, 90 and 110 DMPC lipid molecules and 6, 10, 14, 18, and 22 22A peptide molecules, respectively, maintaining the 1:5 peptide:lipid ratio corresponding to experiments. These systems were simulated with for 10 μs. After placing the molecules into a random configuration for each replicate, the molecules spontaneously self-aggregated into nanodisc particles within 1 μs with DMPC lipid bilayer in the core and 22A peptides on the edges. The final snapshots were converted to atomistic resolution with CHARMM-GUI (45). AMBER systems used Amber ff99SB-ILDN and Lipid17 force fields (46, 47) (as Lipid17 has no published literature a reference to Lipid14 is included) while CHARMM systems used CHARMM36m (48). TIP4P-Ew water model was used in all systems (49). Atomistic simulations were performed using Gromacs version 2020.5 (50). A timestep of 2 fs was used, the temperature was coupled using v-rescale thermostat to 310 K (51), the pressure was set to 1 bar using isotropic Parrinello–Rahman barostat (52), PME was used to calculate electrostatic interactions at distances longer than 1.0 nm (53), and Lennard-Jones interactions were cut off at 1.0 nm.

To create initial configurations for the simulations with picket fence configurations, DMPC lipid bilayers of 20 x 20 nm were created and equilibrated using CHARMM-GUI. Circular cross sections with 70 or 90 lipids were then taken from the equilibrated bilayer. For replicates, the cross sections were taken from different locations. 22A was placed in a circle around the sections in parallel picket fence configuration. The circle radius was 3.5 nm for 70 lipid systems and 4.0 nm for 90 lipid systems.

All systems were first equilibrated for 500 ps with 200 kJ $mol^{-1}nm^{-2}$ and 50 kJ $mol^{-1}nm^{-2}$ restraints on protein backbone and side chains respectively. Then only protein backbone was restrained with 50 kJ $mol^{-1}nm^{-2}$ for 500 ps, and finally without restraints the systems were run for 100 ns. The production systems which were analyzed were run for at least 1 μs.

Calculating spin relaxation times from MD simulations

Spin relaxation times T_1, T_2 and hetNOE values were calculated from simulations, as described previously (36, 54). Briefly, the spectral density, J(w), was calculated as the Fourier transformation of the second-order rotational correlation function C(t) of an N-H peptide bond:

$$J(\omega) = 2\int_0^\infty C(t)\cos(\omega t)\,dt \qquad (1)$$

C(t) was calculated using the Gromacs gmx rotacf module as

$$C(t) = \langle \frac{3}{2} cos^2\theta_{t'+t} - \frac{1}{2} \rangle_{t'} \quad (2)$$

where θ is the angle between the bond in time t′ and time t′ + t. For the Fourier transformation and dynamic landscape analysis, the correlation function C(t) was fitted with a large set of N = 300 exponential functions with predefined timescales τ_i logarithmically spaced between 10 fs and 100 ns as

$$C_{fit}(t) = \sum_{i=1}^{N} \alpha_i e^{-\frac{t}{\tau_i}} \quad (3)$$

where α_i is the weight of a fitted pre-defined timescale τ_i.
The analytical solution of the Fourier transform was used to calculate the spectral density as

$$J_{fit}(\omega) = 2\int_0^{\infty} C_{fit}(t)\cos(\omega t)\, dt = 2\sum_{i=1}^{N} \alpha_i \frac{\tau_i}{1+\omega^2\tau_i^2} \quad (4)$$

Spectral density was then substituted to Redfield equations (54, 55) to calculate spin relaxation times and hetNOE values at the magnetic field of 850MHz corresponding the experimental data.

Calculating SAXS and SANS from MD simulations

Theoretical SAXS and SANS profiles were calculated from MD simulations using CRYSOL (56) and CRYSON (57), respectively. PDB structures were extracted every 10 ns from the simulations and used to calculate scattering curves for the q-range from 0.0085 $Å^{-1}$ to 0.25 $Å^{-1}$ for SAXS and from 0.0094 $Å^{-1}$ to 0.20 $Å^{-1}$ for SANS. Wide-angle regime was not considered as the noise was significant in the experimental curve. Three parameters (the average displaced solvent volume per atomic group, the contrast of the hydration shell and the relative background) were fitted to the experimental curve to account for the solvation layer around the nanodisc and the buffer subtraction. The maximum order of harmonics was set to 30, the electron density of the solvent to 0.334 e/$Å^3$ and the order of Fibonacci grid to 18. Hydrogen atoms were explicitly included.

The quality of the fit to experimental data is determined by the Pearson's chi-squared: $\chi^2 = \sum_i \left(\frac{E_i - C_i}{E_i}\right)^2$, with E_i the experimental values and C_i the calculated values from MD simulation.

Calculating SASA, RMSF and hydrodynamic diameter from MD simulations

Solvent accessible surface areas (SASA) per residue for all peptide atoms were calculated with Gromacs gmx sasa module using standard settings. Root mean square fluctuations (RMSF) were calculated with Gromacs rmsf module by fitting the peptide backbone atoms of each peptide individually to an ideal alpha helical backbone model. Individual per residue RMSF profiles were averaged per system. The average and standard deviation between replicate systems are shown for SASA and RMSF plots. The hydrodynamic diameter was calculated using Hydropro10 software (58) for snapshots generated every 100 ns.

Acknowledgments

We acknowledge the European Synchrotron Radiation Facility (ESRF) for provision of synchrotron radiation facilities under proposal number MX-2582 and we would like to thank Mark Tully for assistance and support in using beamline BM29. We acknowledge the Institut Laue-Langevin (ILL) for provision of neutron radiation facilities and we would like to thank Anne Martel for assistance

and support in using beamline D22. The facilities and expertise of the HiLIFE NMR unit at the University of Helsinki, a member of Instruct-ERIC Centre Finland, FINStruct, and Biocenter Finland are gratefully acknowledged. We acknowledge CSC – IT Center for Science for computational resources. This work was supported by The Academy of Finland [grant numbers 315596, 350636, 353815, 356568].

References

1. H. J. Pownall, C. Rosales, B. K. Gillard, A. M. Gotto, High-density lipoproteins, reverse cholesterol transport and atherogenesis. *Nat Rev Cardiol* **18**, 712–723 (2021).

2. B. A. Kingwell, M. J. Chapman, A. Kontush, N. E. Miller, HDL-targeted therapies: progress, failures and future. *Nat Rev Drug Discov* **13**, 445–464 (2014).

3. G. M. Anantharamaiah, D. Goldberg, Eds., *Apolipoprotein Mimetics in the Management of Human Disease* (Springer International Publishing, 2015).

4. D. Sviridov, A. T. Remaley, High-density lipoprotein mimetics: promises and challenges. *Biochemical Journal* **472**, 249–259 (2015).

5. N. Skar-Gislinge, N. T. Johansen, R. Høiberg-Nielsen, L. Arleth, Comprehensive Study of the Self-Assembly of Phospholipid Nanodiscs: What Determines Their Shape and Stoichiometry? *Langmuir* **34**, 12569–12582 (2018).

6. R. Kuai, D. Li, Y. E. Chen, J. J. Moon, A. Schwendeman, High-Density Lipoproteins: Nature's Multifunctional Nanoparticles. *ACS Nano* **10**, 3015–3041 (2016).

7. F. Hagn, M. L. Nasr, G. Wagner, Assembly of phospholipid nanodiscs of controlled size for structural studies of membrane proteins by NMR. *Nat Protoc* **13**, 79–98 (2018).

8. U. Günsel, F. Hagn, Lipid Nanodiscs for High-Resolution NMR Studies of Membrane Proteins. *Chem. Rev.* **122**, 9395–9421 (2022).

9. T. H. Bayburt, Y. V. Grinkova, S. G. Sligar, Self-Assembly of Discoidal Phospholipid Bilayer Nanoparticles with Membrane Scaffold Proteins. *Nano Lett.* **2**, 853–856 (2002).

10. V. K. Mishra, *et al.*, Association of a Model Class A (Apolipoprotein) Amphipathic α Helical Peptide with Lipid. *Journal of Biological Chemistry* **281**, 6511–6519 (2006).

11. S. R. Midtgaard, *et al.*, Self-assembling peptides form nanodiscs that stabilize membrane proteins. *Soft Matter* **10**, 738–752 (2014).

12. A. N. Larsen, *et al.*, Dimeric peptides with three different linkers self-assemble with phospholipids to form peptide nanodiscs that stabilize membrane proteins. *Soft Matter* **12**, 5937–5949 (2016).

13. J.-L. Dasseux, *et al.*, Apolipoprotein A-I agonist and their use to treat dyslipidemic disorders. (1999).

14. D. Li, S. Gordon, A. Schwendeman, A. T. Remaley, "Apolipoprotein Mimetic Peptides for Stimulating Cholesterol Efflux" in *Apolipoprotein Mimetics in the Management of Human Disease*, G. M. Anantharamaiah, D. Goldberg, Eds. (Springer International Publishing, 2015), pp. 29–42.

538 15. L. Giorgi, *et al.*, Mechanistic Insights into the Activation of Lecithin–Cholesterol
539 Acyltransferase in Therapeutic Nanodiscs Composed of Apolipoprotein A-I Mimetic Peptides
540 and Phospholipids. *Mol. Pharmaceutics* **19**, 4135–4148 (2022).

541 16. A. Niemelä, A. Koivuniemi, Systematic evaluation of lecithin:cholesterol acyltransferase
542 binding sites in apolipoproteins via peptide based nanodiscs: regulatory role of charged residues
543 at positions 4 and 7. *PLoS Comput Biol* **20**, e1012137 (2024).

544 17. M. V. Fawaz, *et al.*, Phospholipid Component Defines Pharmacokinetic and
545 Pharmacodynamic Properties of Synthetic High-Density Lipoproteins. *J Pharmacol Exp Ther*
546 **372**, 193–204 (2020).

547 18. N. Sibille, P. Bernadó, Structural characterization of intrinsically disordered proteins by
548 the combined use of NMR and SAXS. *Biochemical Society Transactions* **40**, 955–962 (2012).

549 19. M. Chan-Yao-Chong, D. Durand, T. Ha-Duong, Molecular Dynamics Simulations
550 Combined with Nuclear Magnetic Resonance and/or Small-Angle X-ray Scattering Data for
551 Characterizing Intrinsically Disordered Protein Conformational Ensembles. *J. Chem. Inf. Model.*
552 **59**, 1743–1758 (2019).

553 20. V. Graziano, L. Miller, L. Yang, Interpretation of solution scattering data from lipid
554 nanodiscs. *J Appl Crystallogr* **51**, 157–166 (2018).

555 21. T. Reddy, J. K. Rainey, Interpretation of biomolecular NMR spin relaxation parameters.
556 *Biochem. Cell Biol.* **88**, 131–142 (2010).

557 22. S. A. Showalter, R. Brüschweiler, Validation of Molecular Dynamics Simulations of
558 Biomolecules Using NMR Spin Relaxation as Benchmarks: Application to the AMBER99SB
559 Force Field. *J. Chem. Theory Comput.* **3**, 961–975 (2007).

560 23. N. Skar-Gislinge, *et al.*, Elliptical Structure of Phospholipid Bilayer Nanodiscs
561 Encapsulated by Scaffold Proteins: Casting the Roles of the Lipids and the Protein. *J. Am. Chem.*
562 *Soc.* **132**, 13713–13722 (2010).

563 24. J. Cavanagh, W. J. Fairbrother, A. G. Palmer III, M. Rance, N. J. Skelton, *Protein NMR*
564 *Spectrocopy (Second Edition)*, Academic Press (2007).

565 25. R. M. Islam, *et al.*, Structural properties of apolipoprotein A-I mimetic peptides that
566 promote ABCA1-dependent cholesterol efflux. *Sci Rep* **8**, 2956 (2018).

567 26. C. Anada, *et al.*, Temperature- and composition-dependent conformational transitions of
568 amphipathic peptide–phospholipid nanodiscs. *Journal of Colloid and Interface Science* **588**, 522–
569 530 (2021).

570 27. S. Inagaki, R. Ghirlando, Nanodisc characterization by analytical ultracentrifugation.
571 *Nanotechnology Reviews* **6**, 3–14 (2017).

572 28. M. Wagner, S. Holzschuh, A. Traeger, A. Fahr, Ulrich. S. Schubert, Asymmetric Flow
573 Field-Flow Fractionation in the Field of Nanomedicine. *Anal. Chem.* **86**, 5201–5210 (2014).

574 29. A. Y. Shih, I. G. Denisov, J. C. Phillips, S. G. Sligar, K. Schulten, Molecular Dynamics
575 Simulations of Discoidal Bilayers Assembled from Truncated Human Lipoproteins. *Biophysical*

576 *Journal* **88**, 548–556 (2005).

577 30. L. R. Kjølbye, *et al.*, General Protocol for Constructing Molecular Models of Nanodiscs.
578 *J. Chem. Inf. Model.* **61**, 2869–2883 (2021).

579 31. T. Bengtsen, *et al.*, Structure and dynamics of a nanodisc by integrating NMR, SAXS and
580 SANS experiments with molecular dynamics simulations. *eLife* **9**, e56518 (2020).

581 32. A. Debnath, L. V. Schäfer, Structure and Dynamics of Phospholipid Nanodiscs from All-
582 Atom and Coarse-Grained Simulations. *J. Phys. Chem. B* **119**, 6991–7002 (2015).

583 33. E. S. Salnikov, G. M. Anantharamaiah, B. Bechinger, Supramolecular Organization of
584 Apolipoprotein-A-I-Derived Peptides within Disc-like Arrangements. *Biophysical Journal* **115**,
585 467–477 (2018).

586 34. S. Bibow, *et al.*, Solution structure of discoidal high-density lipoprotein particles with a
587 shortened apolipoprotein A-I. *Nat Struct Mol Biol* **24**, 187–193 (2017).

588 35. N. Sreerama, R. W. Woody, Estimation of Protein Secondary Structure from Circular
589 Dichroism Spectra: Comparison of CONTIN, SELCON, and CDSSTR Methods with an
590 Expanded Reference Set. *Analytical Biochemistry* **287**, 252–260 (2000).

591 36. R. Nencini, *et al.*, Probing the dynamic landscape of peptides in molecular assemblies by
592 synergized NMR experiments and MD simulations. *Commun Chem* **7**, 28 (2024).

593 37. G. Zhu, Y. Xia, L. K. Nicholson, K. H. Sze, Protein Dynamics Measurements by
594 TROSY-Based NMR Experiments. *Journal of Magnetic Resonance* **143**, 423–426 (2000).

595 38. F. Delaglio, *et al.*, NMRPipe: A multidimensional spectral processing system based on
596 UNIX pipes. *J Biomol NMR* **6** (1995).

597 39. S. P. Skinner, *et al.*, CcpNmr AnalysisAssign: a flexible platform for integrated NMR
598 analysis. *J Biomol NMR* **66**, 111–124 (2016).

599 40. P. Pernot, A. Round, R. Barrett, A. De Maria Antolinos, al., Upgraded ESRF BM29
600 beamline for SAXS on macromolecules in solution. *J Synchrotron Rad* **20**, 660–664 (2013).

601 41. D. Orthaber, A. Bergmann, O. Glatter, SAXS experiments on absolute scale with Kratky
602 systems using water as a secondary standard. *J Appl Crystallogr* **33**, 218–225 (2000).

603 42. S. Förster, L. Apostol, W. Bras, *Scatter* : software for the analysis of nano- and mesoscale
604 small-angle scattering. *J Appl Crystallogr* **43**, 639–646 (2010).

605 43. K. Manalastas-Cantos, *et al.*, *ATSAS 3.0* : expanded functionality and new tools for small-
606 angle scattering data analysis. *J Appl Crystallogr* **54**, 343–355 (2021).

607 44. P. C. T. Souza, *et al.*, Martini 3: a general purpose force field for coarse-grained
608 molecular dynamics. *Nat Methods* **18**, 382–388 (2021).

609 45. S. Jo, T. Kim, V. G. Iyer, W. Im, CHARMM-GUI: A web-based graphical user interface
610 for CHARMM. *J Comput Chem* **29**, 1859–1865 (2008).

611 46. K. Lindorff-Larsen, *et al.*, Improved side-chain torsion potentials for the Amber ff99SB

protein force field. *Proteins* **78**, 1950–1958 (2010).

47. C. J. Dickson, *et al.*, Lipid14: The Amber Lipid Force Field. *J. Chem. Theory Comput.* **10**, 865–879 (2014).

48. J. Huang, *et al.*, CHARMM36m: an improved force field for folded and intrinsically disordered proteins. *Nat Methods* **14**, 71–73 (2017).

49. H. W. Horn, *et al.*, Development of an improved four-site water model for biomolecular simulations: TIP4P-Ew. *The Journal of Chemical Physics* **120**, 9665–9678 (2004).

50. H. J. C. Berendsen, D. Van Der Spoel, R. Van Drunen, GROMACS: A message-passing parallel molecular dynamics implementation. *Computer Physics Communications* **91**, 43–56 (1995).

51. G. Bussi, D. Donadio, M. Parrinello, Canonical sampling through velocity rescaling. *The Journal of Chemical Physics* **126**, 014101 (2007).

52. M. Parrinello, A. Rahman, Polymorphic transitions in single crystals: A new molecular dynamics method. *Journal of Applied Physics* **52**, 7182–7190 (1981).

53. T. Darden, D. York, L. Pedersen, Particle mesh Ewald: An $N \cdot \log(N)$ method for Ewald sums in large systems. *The Journal of Chemical Physics* **98**, 10089–10092 (1993).

54. O. H. S. Ollila, H. A. Heikkinen, H. Iwaï, Rotational Dynamics of Proteins from Spin Relaxation Times and Molecular Dynamics Simulations. *J. Phys. Chem. B* **122**, 6559–6569 (2018).

55. K. T. Dayie, G. Wagner, J.-F. Lefèvre, Theory and Practice of Nuclear Spin Relaxation in Proteins. *Annu. Rev. Phys. Chem.* **47**, 243–282 (1996).

56. D. Svergun, C. Barberato, M. H. J. Koch, *CRYSOL* – a Program to Evaluate X-ray Solution Scattering of Biological Macromolecules from Atomic Coordinates. *J Appl Crystallogr* **28**, 768–773 (1995).

57. D. I. Svergun, *et al.*, Protein hydration in solution: Experimental observation by x-ray and neutron scattering. *Proc. Natl. Acad. Sci. U.S.A.* **95**, 2267–2272 (1998).

58. J. García De La Torre, M. L. Huertas, B. Carrasco, Calculation of Hydrodynamic Properties of Globular Proteins from Their Atomic-Level Structure. *Biophysical Journal* **78**, 719–730 (2000).